Journal of Non-Crystalline Solids 356 (2010) 2714–2721

Contents lists available at ScienceDirect

Journal of Non-Crystalline Solids

journal homepage: www.elsevier.com/ locate/ jnoncrysol

Amorphous niobium oxide thin films

G. Ramírez [a,b], S.E. Rodil [a,*], S. Muhl [a], D. Turcio-Ortega [a], J.J. Olaya [c], M. Rivera [d], E. Camps [e], L. Escobar-Alarcón [e]

[a] Instituto de Investigaciones en Materiales, Universidad Nacional Autónoma de México, Circuito Exterior s/n, CU, México D.F. 04510, México
[b] Facultad de Química, Departamento de Ingeniería Química, Universidad Nacional Autónoma de México, México D.F. 04510, México
[c] Unidad de Materiales, Departamento de Ingeniería Mecánica y Mecatrónica, Universidad Nacional de Colombia, Cra. 30 45-03, Bogotá, Colombia
[d] Instituto de Física, Dpto. Materia Condensada, Universidad Nacional Autónoma de México, CU, México D.F. 04510, México
[e] Departamento de Física, Instituto Nacional de Investigaciones Nucleares, Apdo. Postal 18-1027, México D.F. 11801, México

ARTICLE INFO

Article history:
Received 4 February 2010
Received in revised form 8 September 2010
Available online 11 October 2010

Keywords
Corrosion;
Niobium oxide;
Optical properties;
Mechanical properties;
Amorphous coatings

ABSTRACT

Amorphous niobium oxide thin films were deposited by unbalanced reactive magnetron sputtering under different conditions of pressure (2 to 4 Pa) and oxygen percentage (9, 17, and 23%). The films were characterized to obtain the relationships between the deposition parameters and the most relevant physical properties (structural, optical, mechanical, surface morphology and optical). The composition was determined by Rutherford backscattering spectroscopy and energy dispersive X-ray spectroscopy. From the results of X-ray diffraction and the composition, we can conclude that for all of the deposition pressures and flow ratios used, the films were stoichiometric Nb_2O_5 and amorphous. Similarly, the mechanical and optical properties did not show significant variation between the different deposition conditions; all the films were transparent with a bandgap of about 3.4 eV and a hardness around 5 GPa. Concerning the electrochemical properties, the response of the films to DC polarization in a 0.89% NaCl solution was significantly different. The parameters used to compare the electrochemical response were the polarization resistance and the corrosion resistance obtained from the Tafel analysis.

1. Introduction

Niobium oxide films have been proposed for a wide variety of technological applications, such as sensing materials [1–7], to assist catalytic processes [4,6,8–11] and as biocompatible coatings [12–18]. Since the discovery of electrochromism in 1980, niobium oxide films became promising electrochromic materials for device applications, in part, because of its excellent chemical stability and corrosion resistance in both acid and base media [19–22]. In the microelectronic industry, there has been considerable interest in using transition metal oxides as a high permittivity dielectric to replace SiO_2 in semiconductor devices to increase the charge storage capability and frequency response of devices [23,24]. Niobium oxide has also been proposed as an ideal substitute for Ta_2O_5 in solid electrolyte tantalum/tantalum pentoxide (Ta_2O_5) capacitors, where the oxide dielectric layer is formed from a porous metal powder compacted by anodic oxidation. Due to the larger permittivity of Nb_2O_5 compared to Ta_2O_5 it is a logical substitute since it has a similar anodization behavior and in addition offers the advantage of greater natural abundance and hence, lower raw material price [25–31].

In spite of the large number of applications and interesting properties only a relatively small number of reports are available on the preparation and properties of niobium oxide films. Recent papers describe the preparation by thermal evaporation [32], anodization [26,28,30], sputtering [19,29,33–41], sol–gel processes [42–45], pulsed laser ablation [1,46], spray deposition [22,47], atomic layer deposition [23] and chemical vapor deposition [48].

One difficulty with niobium oxide is the complexity of the crystal system that contains a large variety of polymorphic forms. Additionally, there are at least three stable niobium oxides; NbO, NbO_2 and Nb_2O_5 and each has different electrical properties ranging from conducting NbO to semiconducting NbO_2 and insulating Nb_2O_5 [49].

It has been demonstrated that reactive magnetron sputtering, deposition of niobium oxide at low temperatures leads to an amorphous structure for thicknesses below a critical value [35]. Similarly, it has been shown that the Nb/O composition ratio increases with the relative amount of oxygen in the deposition chamber. However, the specific O_2 content in the gas phase required to obtain a particular composition is difficult to extrapolate from one deposition system to another. The effect of both the deposition pressure and power has been less studied. Magnetron sputtering is a physical vapor deposition process (PVD) classified as a non-equilibrium deposition technique, where the film structure and properties are highly dependent on the deposition parameters, therefore in order to determine the optimum conditions

* Corresponding author.
E-mail address: ser42@iim.unam.mx (S.E. Rodil).

0022-3093/$ – see front matter © 2010 Elsevier B.V. All rights reserved.
doi:10.1016/j.jnoncrysol.2010.09.073

to obtain a specific composition and microstructure, it is necessary to perform a complete characterization of the process condition–properties relationship.

In this paper, we report the results of the deposition of amorphous Nb_2O_5 thin films using an unbalanced magnetron sputtering system. We are particularly interested in evaluating the corrosion protection offered by the amorphous oxide coatings to stainless steel substrates submerged in physiological fluids (0.89% NaCl).

The protection of metals by covering their surface with a non-reactive coating is a good way to take advantage of their mechanical properties while preventing corrosion and introducing one or multiple desirable surface properties in a single step. These properties might be color, wear or corrosion resistance, hardness, electronic insulation, or biocompatibility. Corrosion resistance provided by crystalline sputtered coatings to metallic substrates is affected by the well-known columnar structure of the films deposited at low temperatures [50], and the high density of growth related defects: pores and pinholes [51,52]. The inter-columnar space and defects permit corrosion attack of the substrate (which is usually less noble than the ceramic coating) since they allow the passing of the electrolyte through them. The corrosion is even more severe if the corrosive medium contains chlorine ions (Cl^-) due to the strong ability of Cl^- in promoting localized corrosion.

It has been shown that Nb_2O_5 films have good biological compatibility and are suitable for the surface treatment of implants (e.g. prostheses) [13,16,53]. However, these applications require the parts to be exposed to an environment which contains a wide range of chemical reagents or corrosive liquids. Therefore, failure of coatings is often connected to corrosive attack which reduces the lifetime and service quality of the coated parts, despite the fact that the coating materials themselves are highly corrosion resistant [54].

Thus, the fact that our as-grown Nb_2O_5 films are amorphous, with no columns, can be expected to help in reducing attack by corrosion. To a large extent this is the motivation of the present work: produce amorphous Nb_2O_5 films on stainless steel substrates and evaluate the corrosion resistance in a physiological fluid.

The paper is divided in two parts; the first concerns the identification of the deposition parameters that lead to the amorphous niobium pentoxide phase and the second, to the evaluation of the functional properties, i.e., the corrosion resistance.

2. Materials and methods

2.1. Film deposition

The niobium oxide films were deposited using a commercial unbalanced magnetron, a Nb target (0.1 m diameter, 99.95% purity), in $Ar + O_2$ (both of ultra high purity) atmosphere. The equipment has an automated gas flow system that maintained the deposition pressure constant while the O_2 flow ratio was increased from 9 to 23%. The samples were deposited simultaneously on pieces of crystalline silicon (111) and AISI 316L stainless steel substrates (SS) polished with 600 grade SiC grit. The base pressure in the system was 5×10^{-4} Pa and the substrate–target distance was 0.05 m. The DC sputtering power was fixed at 80 W and both the gas pressure and percentage of oxygen in the gas phase were varied as described in Table 1. The O_2% was relatively high in order to avoid the formation of lower oxygen content niobium oxides, such as NbO and NbO_2 [36]. The deposition time was adjusted to obtain samples of 200 nm thickness for all of the conditions used; the deposition rates obtained from an average of five measurements are shown in Table 1.

2.2. Film characterization

The film structure was analyzed by X-ray diffraction (XRD) using a Siemens D500 system in grazing angle (incidence angle 2°) mode and CuKα radiation. The chemical composition of the films was measured by both energy dispersive X-ray (EDX) and Rutherford backscattering spectroscopy (RBS). The RBS analysis was carried out using 5 MeV Li^{2+} ion beam from a Tandem Van de Graff accelerator and 135° detection angle [55]. The EDX spectra were obtained in a scanning electron microscope (SEM) Cambridge-Leica Stereo Scan 440 system. Selected samples were first analyzed by RBS to obtain the Nb and O atomic concentrations, then the same samples were used as standard to obtain sensitivity factors for EDX analysis of the Nb and O atomic concentrations of the other samples [56].

The film hardness was measured using a Nano-Hardness Tester from CSM with a Berkovich indenter and a load of 0.3 mN. More than five indentations were made on each sample to obtain the average film hardness and the standard deviations.

The surface morphology was studied using an atomic force microscopy (AFM) Jeol JSPM-4210 in tapping mode with a velocity of 1.6667/ms.

The optical properties, the thickness and the optical-roughness of the films were obtained by spectroscopy ellipsometry. The measurements were carried out ex-situ using a Horiba Jobin Yvon spectroscopic ellipsometer using three incidence angles (60°, 65°, and 70°) and a photon-energy range of 1.5–4.5 eV with an interval step of 0.05 eV.

Samples deposited on the silicon substrates were used for the optical, mechanical, structural and compositional measurements. The corrosion resistance analysis was evaluated using films deposited on AISI 316 stainless steel discs.

The corrosion resistance was evaluated by potentiodynamic anodic polarization. The tests were performed, in triplicate, on the bare and coated stainless steel substrates. The counter electrode was a platinum wire and the reference was a saturated calomel electrode (SCE). The electrolyte was 8.9 g/l NaCl, pH 7.4. The sample was sealed to the wall of the electrochemical apparatus with a Viton O-ring leaving an area of 0.1 cm^2 exposed to the solution. The sample was kept in contact with the electrolyte solution at room temperature for 1 h to obtain the open circuit potential (OCP). Then, the voltage was scanned from −280 mV vs. OCP to +1280 mV vs. OCP at a scan rate of 20 mV/min.

As support to the DC electrochemical testing, we also performed electrochemical impedance spectroscopy (EIS) in the frequency range from 10 kHz to 1 mHz, after 2 h of immersion in the NaCl electrolyte. Five data points per decade were measured at an amplitude of 10 mV. The impedance spectra were analyzed using standard equivalent circuits for thin films on metal substrates. The EIS and potentiodynamic polarization measurements were carried out using a Gamry Instruments potentiostat, Framework 2004, Version 5.3.

Table 1
Deposition conditions and properties of the series of NbO_x films.

Sample name	NbO_x-01	NbO_x-02	NbO_x-03	NbO_x-04	NbO_x-05	NbO_x-06	NbO_x-07	NbO_x-08	NbO_x-09
Pressure (Pa)	2	2	2	3	3	3	4	4	4
O_2 %	9	17	23	9	17	23	9	17	23
Nb/O	0.390	0.429	0.430	0.394	0.417	0.418	0.418	0.394	0.429
Growth rate (nm/s)	0.160 ± 0.002	0.140 ± 0.005	0.120 ± 0.005	0.130 ± 0.003	0.120 ± 0.2	0.100 ± 0.002	0.120 ± 0.003	0.110 ± 0.005	0.090 ± 0.003
Hardness (GPa)	3.9 ± 0.1	5.3 ± 0.7	4.9 ± 1.0	3.9 ± 0.4	4.8 ± 0.5	4.5 ± 0.8	4.0 ± 0.2	4.4 ± 0.3	4.3 ± 0.7
Band gap *Eg* (eV)	3.35 ± 0.01	3.40 ± 0.01	3.41 ± 0.01	3.40 ± 0.01	3.46 ± 0.01	3.40 ± 0.01	3.45 ± 0.01	3.36 ± 0.01	3.41 ± 0.01
Refractive index at 2.25 eV	2.27	2.30	2.25	2.26	2.27	2.25	2.21	2.23	2.24

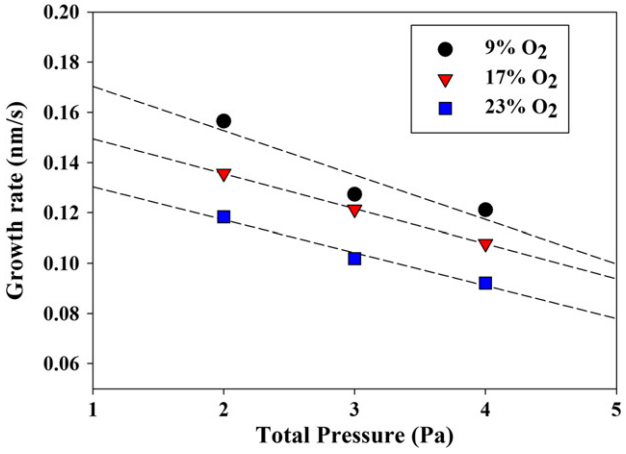

Fig. 1. Variation of the deposition rate as a function of the pressure for the three different O_2%. The lines are only guides for the eyes.

All experimental results, were analyzed using statistical analysis based on the Bonferroni's test using $p<0.05$ to find correlation between the deposition conditions and properties.

3. Results and discussion

3.1. Deposition parameters — properties

Fig. 1 shows the deposition rates as a function of the deposition pressure for the three different O_2%. It can be seen that the rate decreased as both the amount of O_2 and/or the pressure increased. This is in good agreement with other experimental results and is characteristic of reactive magnetron sputtering [36,57].

Fig. 2 shows typical XRD spectra of the films and the absence of the diffraction peaks confirms their amorphous nature. Fig. 2 also includes the XRD spectra of samples annealed for 1 h in air at 400 and 500 °C. In agreement with other authors, crystallization occurs at temperatures above 400 °C and the 500 °C annealed sample clearly showed diffraction peaks corresponding to the hexagonal Nb_2O_5 phase (JCPDS 28-0317) [58].

The RBS spectra and composition of one of the samples is shown in Fig. 3. As mentioned above, the compositions obtained from RBS were used to calibrate the EDX spectra and to obtain the Nb/O composition ratio for the 9 samples which are given in Table 1. Somewhat surprisingly, all the Nb/O ratios ranged between 0.390 and 0.429 without any clear trend with the preparation conditions.

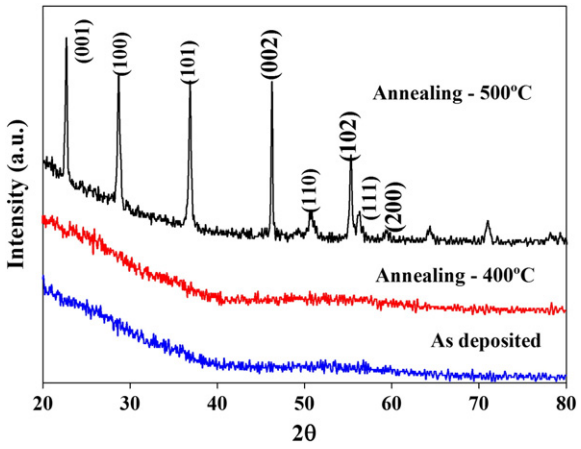

Fig. 2. Typical diffraction patterns for the amorphous films. The spectra of two samples annealed in air at 400 and 500 °C are also included. The diffraction planes corresponding to the hexagonal Nb_2O_5 phase are clearly observed for the 500 °C annealed sample.

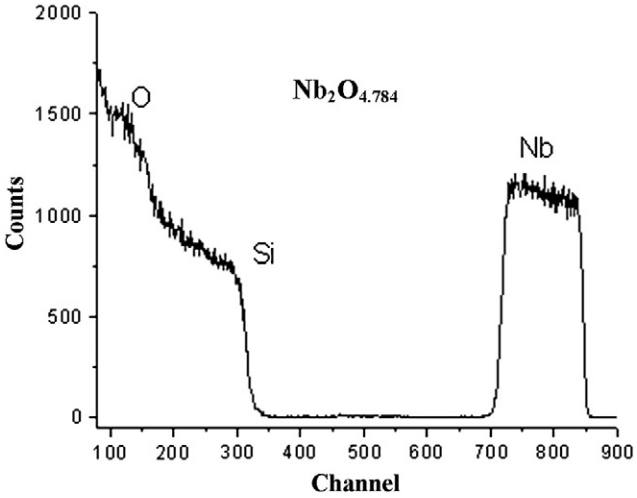

Fig. 3. RBS spectra of a NbO_x-06 sample showing a composition, obtained from the simulation of the spectra, very close to Nb_2O_5.

The hardness was obtained by nanoindentation using very low loads to avoid a large penetration of the indenter. Nevertheless, since the samples were very thin the penetration was about 25% of the total thickness. The results are shown in Fig. 4 as a function of the pressure and for the different O_2 fractions. The statistical analysis made, using the Bonferroni's test, showed no significant difference between the hardness of the nine coatings. The large deviations are probably related to inhomogeneities in the sample surface, since variability did not improve by increasing the number of measurements. The hardness values ranged between 3.9 ± 0.1 GPa and 5.3 ± 0.7 GPa. There are few papers that report the hardness of Nb_xO_y; Chappe et al. [59] mentioned values of about 6 GPa and in a more recent paper Cetinorgu et al. [33] measured the hardness of amorphous Nb_2O_5 films deposited by dual ion beam sputtering as a function of the ion energy and the values ranged between 5.5 and 6.5 GPa.

The surface morphology of some of the samples deposited on silicon substrates is shown in Fig. 5. It can be observed that the topography changed as the deposition conditions varied, but again no clear trends were found. The RMS roughness varied from 1.1 to 6.4 nm, which are values similar to those reported for sputtering deposition [35].

The typical measured ellipsometry spectra (dots) of Si/Nb_2O_5 films are presented in Fig. 6 together with their best-fit curves (lines). The ellipsometry spectra are reported as I_s and I_c, which are the experimental measurements in a phase modulated ellipsometer [60]. These spectra

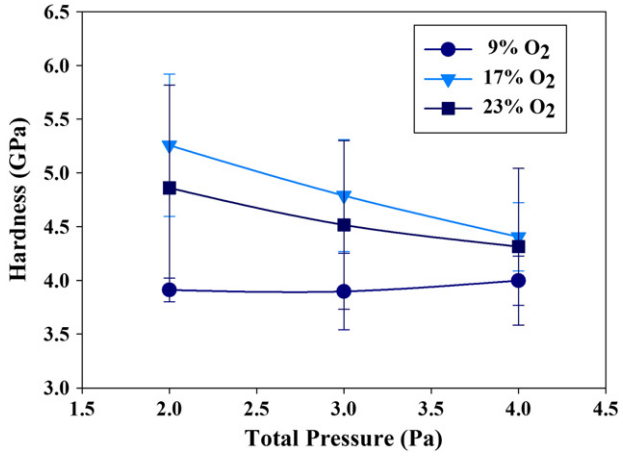

Fig. 4. Variation of the hardness of the Nb_2O_5 films as a function of the pressure for the three different O_2%. The lines are guides for the eyes.

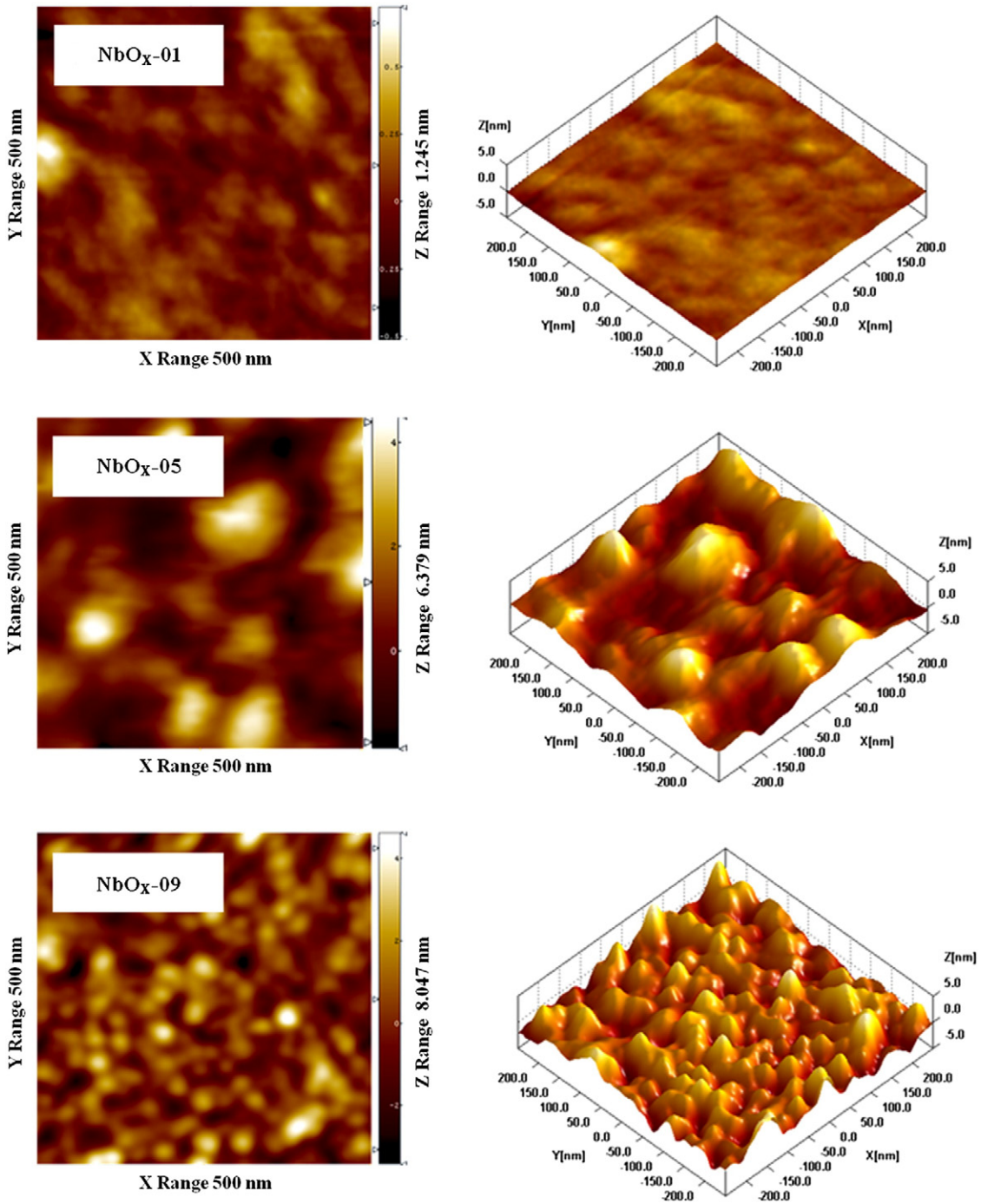

Fig. 5. Surface morphology of selected samples obtained by atomic force microscopy.

correspond to the experimental data for three incident angles for the sample NbO_x-01. In the analysis of the experimental ellipsometry spectra, the dispersion function used to parameterize the complex dielectric functions of the Nb_2O_5 films was the Tauc–Lorentz function proposed by Jellison and Modine [61], which is the combination of the Tauc joint density of states and the quantum mechanical Lorentz oscillator (two oscillators were used) model and satisfies the Kramers–Kronig relation. Additionally, we assumed a two-layer structure: a top layer to take into account the surface roughness (50% Nb_2O_5 + 50% void) and a second layer of Nb_2O_5 modeled by the Tauc–Lorentz function. The actual determination of the model parameters was carried out using the Levenberg–Marquardt algorithm to minimize the difference between the measured and fitted spectra. The fittings carried out using the model and dispersion function described above are shown as lines in Fig. 6. The calculated values of the film thickness agreed well with those measured by profilometry for all of the samples.

As result of the modeling of the nine films, the refractive index and extinction coefficient dispersion were obtained and the values are shown in Fig. 7. The inset shows that there was a slight increment of the refractive index as the pressure was decreased suggesting a densification of the films at a lower pressure as also found by other authors. The optical gap (the photon energy at which extinction coefficient, k, is greater than zero; according to the definition from the Tauc–Lorentz model) was between 3.35 and 3.46 eV. The error associated to the optical gap value given in Table 1 is the parameter from the minimization algorithm.

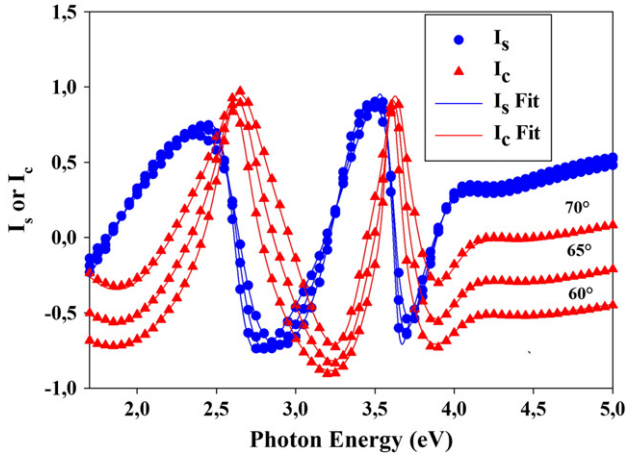

Fig. 6. Measured (dots) and fitted (lines) values of the ellipsometric data; I_s and I_c for the three different acquisition angles, I_s and I_c are correlated to the ellipsometric parameters as $I_s = \sin 2\Psi \sin\Delta$ and $I_c = \sin 2\Psi \cos\Delta$. The three spectra were fitted simultaneously to obtain the film optical parameters, thickness and roughness of the layer. The figure of merit (Levenberg–Marquardt algorithm) for fitting the three angles and the complete energy range (1.5–5 eV) was between 1.8 and 9 for all samples.

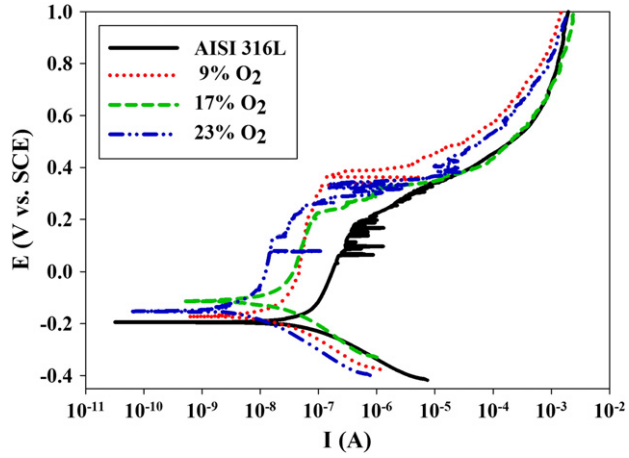

Fig. 8. Potentiodynamic polarization curves for films obtained at 2 Pa and different O_2% in comparison to the stainless steel substrate. The electrolyte was 0.89% NaCl at pH 7.4, simulating body fluid saline content.

3.2. Functional properties: corrosion resistance

For clarity Fig. 8 only shows the polarization curves for the samples deposited at 2 Pa in comparison to the SS substrate. It can be seen that all the coatings showed a more noble behavior than the SS substrate. The scans were made up to 1280 mV vs. OCP (open circuit potential) to observe the passivation region and failure of the surfaces. It can be seen that the passivation zone is more extended for the coated substrate. The results of the Tafel analysis made over the interval (−250 mV, 250 mV), around OCP and the polarization resistance within the interval (−10, 10 mV) are shown in Fig. 9 for all of the samples. It can be seen that the NbO_x-06 and NbO_x-02 coatings have the largest polarization resistance (R_p) and the smallest current

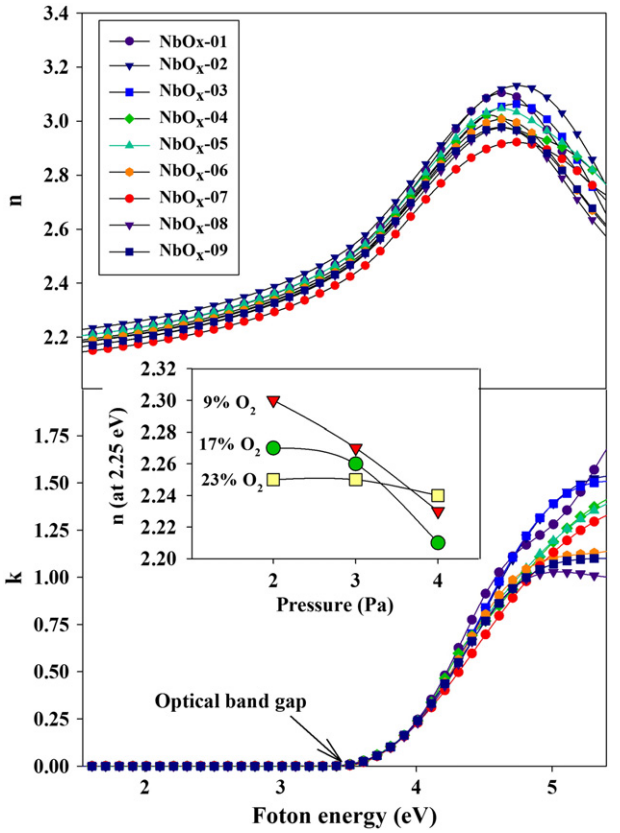

Fig. 7. The film optical parameters; refractive index and extinction coefficient as a function of the photon energy. The inset shows the variation of the refractive index at 2.25 eV as a function of the deposition pressure.

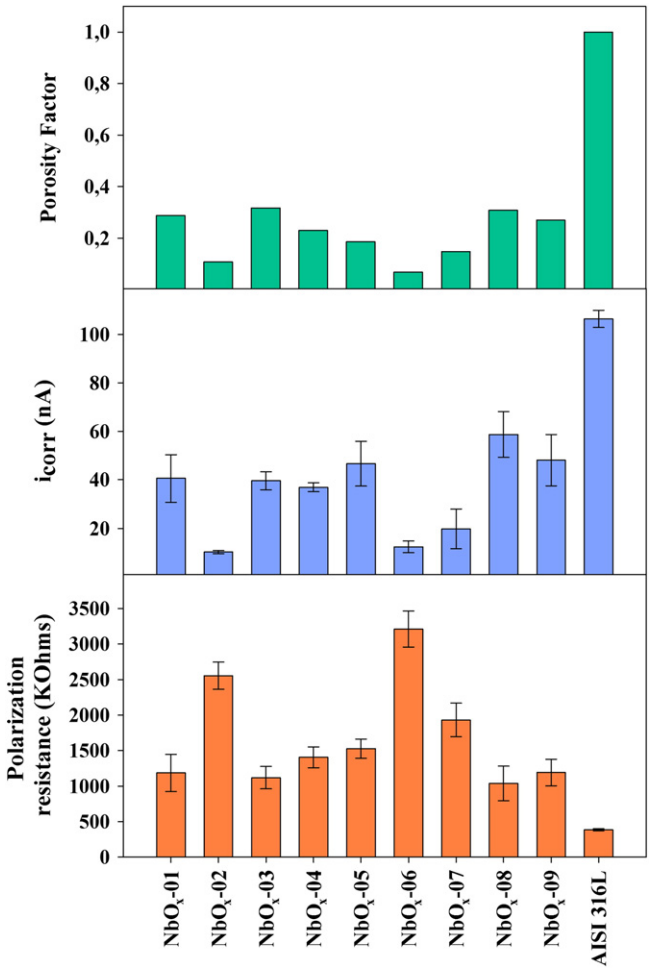

Fig. 9. Results from the electrochemical characterization tests for all samples and the substrate. The top plot shows the porosity factor estimated from the equation shown in the text, the middle plot corresponds to the corrosion current obtained from the Tafel analysis and the bottom plot is the polarization resistance.

density (I_{corr}). Moreover, the porosity (P) was much reduced for these films; P was estimated using the following equation [62]

$$P = \left(R_{pm} / R_p\right) 10^{-|\Delta E_{corr}| / \beta a}$$

where R_{pm} is the polarization resistance of the bare stainless steel, R_p is the polarization resistance of the coating, β_a is the anodic Tafel slope of the bare stainless steel and ΔE_{corr} is the difference in corrosion potential between the coated and bare substrate again using data obtained from the Tafel analysis. The electrochemical determination of the coating porosity is based on the idea that the pores in the coating provide a passage through which the exposed substrate can react with the electrolyte. According to this analysis, the film which gave the best corrosion protection was NbO_x-6 (minimum porosity factor 0.07). This sample was used to measure the impedance spectra of the coating in comparison to the substrate.

The values of impedance over a wide frequency range (EIS data) were analyzed by Bode plots, see Fig. 10. The EIS spectra show that the impedance at the lowest frequency, Z_{mod}, is larger for the coating than for the substrate confirming the higher resistance from the Nb_2O_5 film. The two materials showed a capacitive response with a phase angle close to −80°. Moreover, for the coating, two time constants can be clearly observed.

4. Discussion

4.1. Film properties

The composition, structure, mechanical and optical characterization of the nine niobium oxide films indicated that they were amorphous with a composition close to Nb_2O_5 and, that within the range of deposition conditions used, no significant variations of the properties were seen. The fact that we did not detect significant changes in the film composition, structure and physical properties as a function of either the O_2% or the gas pressure may be because the three O_2 fractions were sufficiently high to cause the target surface to be fully oxidized and therefore, the deposit was always of the more stable Nb_2O_5 phase.

The hardness of the Nb_2O_5 amorphous films was between 4 and 5 GPa. The measurements were made by nanoindentation with a maximum penetration depth close to 25% of the thickness and the hardness values were obtained using the Oliver–Pharr (O–P) method. It is not clear if these values correspond to the "true" film hardness since it has been well-established that the hardness of thin films depends on the penetration depth due to the influence of the substrate. A common rule is to limit the indentation depth to less than 10% of the film thickness and this is generally used for the characterization of hard films deposited on soft substrates. However, in our case, the hardness of the Nb_2O_5 films is lower than the hardness of the silicon substrates (9–12 GPa depending on orientation) [63]. In this situation there are some controversies about the applicability of the 10% limit. It has been shown that there is an error in the estimation of the contact area because of material pile-up around the indenter, instead of sink-in as assumed in the O–P method [64]. However, it seems that the substrate-effects are observed for penetration depths slightly larger than 10%. Saha et al. [65] found that the "true" hardness of aluminum films on different hard substrates could be obtained for $0.05 < h/t < 0.2$, where h is the penetration and t the film thickness. Similarly, Pelegri and Haung [66] by finite element analysis found a "true" hardness for h/t between 0.05 and 0.45, while Beegan et al. [63] reported the influence of the substrate for all h/t values. Thus considering that it was not possible to measure indentations below $h/t = 0.25$, the reported hardness in this work might be somewhat overestimated. However, given that our films were all of the same thickness and were deposited on the same substrate, the associated systematic error is the same for all of them. Thus, we can conclude that the hardness did not vary significantly within the range of experimental conditions studied, and that they were lower than those reported by Cetinorgu et al. [33].

4.2. Corrosion resistance

The electrochemical impedance spectroscopy was used to evaluate more carefully the corrosion resistance of the best coating (NbO_x-06) determined by the potentiodynamic test in comparison to the bare substrate. Fig. 10 shows the impedance spectra, where three different regions can be observed; high (10^4–10^2), medium (10^2–10^{-1}) and low frequency ($<10^{-1}$), which reflect the behavior of the different interfaces of the samples. This behavior can be modeled using equivalent electrical circuits, as shown in Fig. 11 for the uncoated and coated substrate. In these circuits, R_{sol} represents the resistance of the solution between the working (sample) and the reference electrode, i.e. the ohmic drop across the electrolyte. For the SS, it

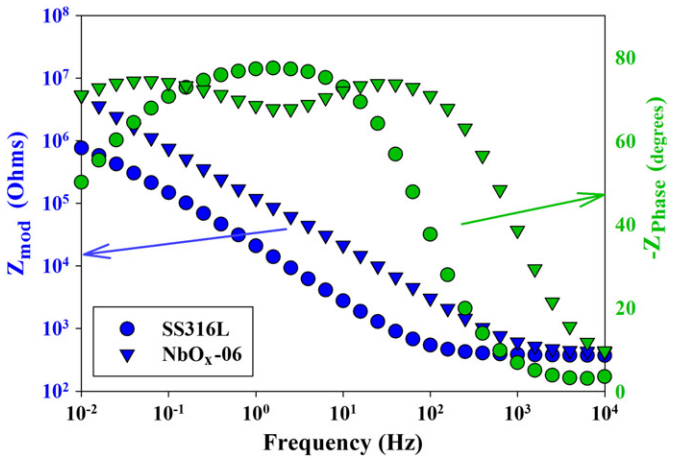

Fig. 10. Bode plot showing the modulus and phase of the impedance as a function of the frequency for sample NbO_x-06 and the bare substrate. The maxima in the phase angle are correlated to the coating–electrolyte and substrate–coating interfaces.

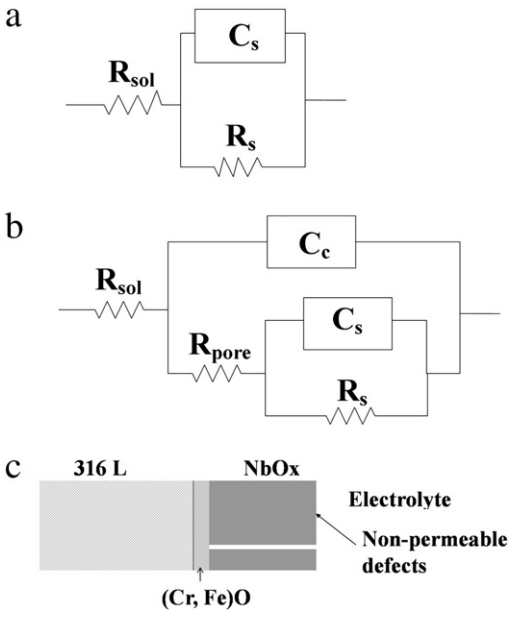

Fig. 11. Equivalent circuits used to analyze the EIS spectra for; a) the uncoated stainless steel, b) the coated substrate and c) the schematic representation of the different interfaces observed in the Bode plot in Fig. 10.

Table 2
Results obtained from fitting the EIS spectra using the equivalent circuit shown in Fig. 11. The resistance and capacitance are defined in Fig. 11 and in the text, while the n factors correspond to the exponent of the constant phase elements (CPE) used to fit the non-ideal capacitors. The impedance of a CPE is defined as: $\frac{1}{Z_{CPE}} = Q^*(j\omega)^n$ where Z_{CPE} is the impedance of the CPE, Q is a proportional factor, ω is the angular frequency, and n is a factor which represents the degree of non-ideality (if n is equal to 1 then we have an ideal capacitor). The Levenberg–Marquardt method indicated that the correctness of fit was 6.25×10^{-4}.

	SS316L	NbO_x-06
R_{sol} (Ω)	366.8	404.8
R_s (Ω)	1.62E+06	1.05E+07
C_s (S^*s^n)	1.03E−05	8.28E−07
n_s	8.67E−01	8.24E−01
R_{pore}	–	1.74E+05
C_c (S^*s^n)	–	1.17E−06
n_c	–	8.79E−01

has been shown that a simple RC circuit can be used, where R_s is the charge transfer resistance and C_s is the double layer capacitance [67]. On the other hand, the circuit shown in Fig. 11b has been proposed to describe protective coatings on metallic substrates [51]. Here, the capacitance of the perfect coating is represented by C_c, with a value much smaller than that typical for the double layer capacitance, and ion conduction paths in the coatings due to the presence of pores or defects are represented by R_{pore} (schematically shown in Fig. 11c). The pore resistance is in series with the parallel RC contribution of the substrate. These capacitances are mathematically modeled by a constant phase element to take into account the inhomogeneities in the surface. The total interfacial impedance (Z) measured at very low frequency, LF, provides a measure of the protective nature of the coatings. At a high frequency, HF, the changes of C_c with the exposure time can be used to determine degradation of the coatings. Similarly, the decrease of R_{pore} in the medium frequency range, MF, also indicates the coating degradation; these processes will be studied as a function of immersion time in the future. For the present paper, using a single immersion time, it is possible to use the polarization resistance, R_p, estimated from EIS to appreciate the effect of the film on the corrosion resistance of the steel substrate. The R_p is defined as the sum of the corresponding resistances; for the single substrate $R_p = R_s$ and for the coated substrate $R_p = R_{pore} + R_s$, where the inverse of the R_p is proportional to the corrosion rate.

Thus, the EIS spectra of Fig. 10 show that the impedance, Z_{mod}, is larger for the coating than for the substrate, confirming the higher resistance provided by the Nb_2O_5 film. Moreover, the numerical results (Table 2) obtained from the fitting procedure showed that R_p for the film is one order of magnitude larger than for the bare substrate, therefore the corrosion rate of the stainless steel was decreased by the deposition of the 200 nm Nb_2O_5 amorphous film.

In the future, we plan to prepare crystalline Nb_2O_5 coatings to compare electrochemical response with that of the amorphous films. It was not possible to use the 500 °C annealed samples because the films showed clear evidence of cracking. On the other hand, the good corrosion protection shown by the amorphous films grown without substrate heating or thermal treatments is of industrial interest for applications where the substrate cannot stand high temperatures or simply to reduce process costs.

5. Conclusions

Amorphous niobium oxide films have been prepared by reactive DC magnetron sputtering on Si and stainless steel substrates at different oxygen percentages and pressures. From the RBS and EDX measurements it was found that the films were amorphous with a composition very close to stoichiometric Nb_2O_5, suggesting deposition from a fully oxidized Nb target. It was shown that deposition from O_2 concentrations between 9 and 23% and pressures from 2 to 4 Pa produced films which are relatively smooth, fully transparent (~3.4 eV), have a high-refractive index (~2.3 at 2.25 eV) and a hardness of about 5 GPa. The deposition rate decreased from 0.18 to 0.09 nm/s as either the O_2% or the pressure was increased. Moreover, from the point of view of corrosion resistance not all the deposition conditions were equivalent. For example the corrosion porosity factor changed by two orders of magnitude for specific deposition conditions, suggesting that some films had much fewer defects and thus provided better corrosion protection even though the physical–chemical properties were indistinguishable.

Acknowledgements

Special thanks for assistance of academic technicians; H. Zarco and S. Romero. We wish to acknowledge the financial support from DGAPA-UNAM IN103910. G. Ramírez acknowledges CONACYT for his PhD scholarship.

References

[1] M.E. Gimon-Kinsel, K.J. Balkus, Microporous and Mesoporous Materials 28 (1999) 113.
[2] S. Rho, D. Jahng, J.H. Lim, J. Choi, J.H. Chang, S.C. Lee, K.J. Kim, Biosensors & Bioelectronics 23 (2008) 852.
[3] S.B. Ficarro, J.R. Parikh, N.C. Blank, J.A. Marto, Analytical Chemistry 80 (2008) 4606.
[4] T. Tamai, M. Haneda, T. Fujitani, H. Hamada, Catalysis Communications 8 (2007) 885.
[5] P. Luo, Y. Liu, G.M. Xie, X.L. Xiong, S.X. Deng, F.Z. Song, Forensic Science International 179 (2008) 192.
[6] U. Cvelbar, M. Mozetic, Journal of Physics D-Applied Physics 40 (2007) 2300.
[7] R. Binions, C.J. Carmalt, I.P. Parkin, Measurement Science & Technology 18 (2007) 190.
[8] A.G.S. Prado, L.B. Bolzon, C.P. Pedroso, A.O. Moura, L.L. Costa, Applied Catalysis B-Environmental 82 (2008) 219.
[9] L.C.A. Oliveira, T.C. Ramalho, M. Goncalves, F. Cereda, K.T. Carvalho, M.S. Nazzarro, K. Sapag, Chemical Physics Letters 446 (2007) 133.
[10] T. Shishido, T. Miyatake, K. Teramura, Y. Hitomi, H. Yamashita, T. Tanaka, Journal of Physical Chemistry C 113 (2009) 18713.
[11] K. Tanabe, Catalysis Today 28 (1996) 1.
[12] E. Eisenbarth, D. Velten, J. Breme, Biomolecular Engineering 24 (2007) 27.
[13] E. Eisenbarth, D. Velten, M. Muller, R. Thull, J. Breme, Journal of Biomedical Materials Research Part A 79A (2006) 166.
[14] V.V. Starikov, S.L. Starikova, A.G. Mamalis, S.N. Lavrynenko, J.J. Ramsden, Journal of Biological Physics and Chemistry 7 (2007) 141.
[15] M.T. Tanvir, Y. Aoki, H. Habazaki, Applied Surface Science 255 (2009) 8383.
[16] R.L. Karlinsey, A.T. Hara, K. Yi, C.W. Duhn, Biomedical Materials 1 (2006) 16.
[17] R.L. Karlinsey, K. Yi, Journal of Materials Science-Materials in Medicine 19 (2008) 1349.
[18] A. Ochsenbein, F. Chai, S. Winter, M. Traisnel, J. Breme, H.F. Hildebrand, Acta Biomaterialia 4 (2008) 1506.
[19] Y.S. Huang, Y.Z. Zhang, X.F. Hu, Journal of Inorganic Materials 17 (2002) 632.
[20] M. Macek, B. Orel, Solar Energy Materials and Solar Cells 54 (1998) 121.
[21] S.H. Mujawar, A.I. Inamdar, C.A. Betty, V. Ganesan, P.S. Patil, Electrochimica Acta 52 (2007) 4899.
[22] S.H. Mujawar, A.I. Inamdar, S.B. Patil, P.S. Patil, Solid State Ionics 177 (2006) 3333.
[23] K. Kukli, M. Ritala, M. Leskela, Journal of the Electrochemical Society 148 (2001) F35.
[24] S. Venkataraj, D. Severin, S.H. Mohamed, J. Ngaruiya, O. Kappertz, M. Wuttig, Thin Solid Films 502 (2006) 228.
[25] S.M. Jung, I.S. Bae, J.S. Yoon, S. Goto, B.I. Kim, Materials Transactions 48 (2007) 3197.
[26] H. Stormer, A. Weber, V. Fischer, E. Ivers-Tiffee, D. Gerthsen, Journal of the European Ceramic Society 29 (2009) 1743.
[27] J.S. Yoon, S.W. Cho, Y.S. Kim, B.I. Kim, Metals and Materials International 15 (2009) 405.
[28] J. Choi, J.H. Lim, J. Lee, K.J. Kim, et al., Nanotechnology (2007) 18.
[29] H. Habazaki, T. Ogasawara, H. Konno, K. Shimizu, S. Nagata, K. Asami, K. Takayama, P. Skeldon, G.E. Thompson, Journal of the Electrochemical Society 153 (2006) B173.
[30] R.L. Karlinsey, Electrochemistry Communications 7 (2005) 1190.
[31] V.A. Matylitskaya, W. Bock, B.O. Kolbesen, Analytical and Bioanalytical Chemistry 390 (2008) 1507.
[32] M.T. Duffy, C.C. Wang, A. Waxman, K.H. Zaininge, Journal of the Electrochemical Society 116 (1969) 234.
[33] E. Cetinorgu, B. Baloukas, O. Zabeida, J.E. Klemberg-Sapieha, L. Martinu, Applied Optics 48 (2009) 4536.
[34] M.G. Krishna, A.K. Bhattacharya, International Journal of Modern Physics B 13 (1999) 411.
[35] F.C. Lai, L.M. Lin, Z.G. Huang, R.Q. Gai, Y. Qu, Applied Surface Science 253 (2006) 1801.

[36] S. Venkataraj, R. Drese, O. Kappertz, R. Jayavel, M. Wuttig, Physica Status Solidi a-Applied Research 188 (2001) 1047.
[37] K. Yoshimura, T. Miki, S. Tanemura, Journal of the Electrochemical Society 144 (1997) 2982.
[38] M. Vinnichenko, A. Rogozin, D. Grambole, F. Munnik, A. Kolitsch, W. Moller, O. Stenzel, S. Wilbrandt, A. Chuvilin, U. Kaiser, Applied Physics Letters (2009) 95.
[39] M.T. Tanvir, K. Fushimi, Y. Aoki, H. Habazaki, Materials Transactions 49 (2008) 1320.
[40] M. Serenyi, T. Lohner, P. Petrik, Z. Zolnai, Z.E. Horvath, N.Q. Khanh, Thin Solid Films 516 (2008) 8096.
[41] B. Hunsche, M. Vergohl, H. Neuhauser, F. Klose, B. Szyszka, T. Matthee, Thin Solid Films 392 (2001) 184.
[42] M. Macek, B. Orel, Turkish Journal of Chemistry 22 (1998) 67.
[43] M. Mirzaee, M.M. Amini, M. Sadeghi, F.Y. Mousavi, M. Sharbatdaran, Ceramics-Silikaty 49 (2005) 40.
[44] N. Ozer, M.D. Rubin, C.M. Lampert, Solar Energy Materials and Solar Cells 40 (1996) 285.
[45] M. Schmitt, S. Heusing, M.A. Aegerter, A. Pawlicka, C. Avellaneda, Solar Energy Materials and Solar Cells 54 (1998) 9.
[46] Z.W. Fu, J.J. Kong, Q.Z. Qin, Journal of the Electrochemical Society 146 (1999) 3914.
[47] P.S. Patil, A.R. Patil, S.H. Mujawar, S.B. Sadale, Journal of Materials Science-Materials in Electronics 16 (2005) 35.
[48] J.P. Masse, H. Szymanowski, O. Zabeida, A. Amassian, J.E. Klemberg-Sapieha, L. Martinu, Thin Solid Films 515 (2006) 1674.
[49] K. Tanabe, Catalysis Today 78 (2003) 65.
[50] I. Petrov, P.B. Barna, L. Hultman, J.E. Greene, Journal of Vacuum Science & Technology A 21 (2003) S117.
[51] C. Liu, Q. Bi, A. Leyland, A. Matthews, Corrosion Science 45 (2003) 1243.
[52] C. Liu, Q. Bi, A. Leyland, A. Matthews, Corrosion Science 45 (2003) 1257.
[53] X.J. Wang, Y.C. Li, J.G. Lin, Y. Yamada, P.D. Hodgson, C.E. Wen, Acta Biomaterialia 4 (2008) 1530.
[54] D.B. Camovska, M.L. Arsov, T.P. Grcev, Macedonian Journal of Chemistry and Chemical Engineering 26 (2007) 95.
[55] S. Romero, M. Fernandez, G. Murillo, H.M. Berdejo, Nuclear Instruments & Methods in Physics Research Section B-Beam Interactions with Materials and Atoms 194 (2002) 164.
[56] D. Bach, R. Schneider, D. Gerthsen, Microscopy and Microanalysis 15 (2009) 524.
[57] D. Depla, J. Haemers, R. De Gryse, Thin Solid Films 515 (2006) 468.
[58] International Centre for Diffraction Data, Joint Committee on Powder Diffraction Standards Database.
[59] J.M. Chappe, P. Carvalho, S. Lanceros-Mendez, M.I. Vasilevskiy, F. Vaz, A.V. Machado, M. Fenker, H. Kappl, N.M.G. Parreira, A. Cavaleiro, E. Alves, Surface & Coatings Technology 202 (2008) 2363.
[60] B. Drevillon, Progress in Crystal Growth and Characterization of Materials 27 (1993) 1.
[61] G.E. Jellison, F.A. Modine, Applied Physics Letters 69 (1996) 371.
[62] Y.M. Chen, G.P. Yu, J.H. Huang, Surface & Coatings Technology 150 (2002) 309.
[63] D. Beegan, S. Chowdhury, M.T. Laugier, Thin Solid Films 466 (2004) 167.
[64] R. Saha, W.D. Nix, Materials Science and Engineering a-Structural Materials Properties Microstructure and Processing 319 (2001) 898.
[65] R. Saha, W.D. Nix, Acta Materialia 50 (2002) 23.
[66] A.A. Pelegri, X. Huang, Composites Science and Technology 68 (2008) 147.
[67] D.A. Lopez, A. Duran, S.M. Cere, Journal of Materials Science-Materials in Medicine 19 (2008) 2137.